A-site order-disorder in the $NdBaMn_2O_{5+\delta}$ SOFC electrode material monitored *in-situ* by neutron diffraction under hydrogen flow

Florent Tonus[1], Mona Bahout[2], Vincent Dorcet[2], Rakesh K. Sharma[3], Elisabeth Djurado[3] Serge Paofai[2], Ronald I. Smith[4], and Stephen J. Skinner[1*]*

[1] Department of Materials, Imperial College London, Exhibition Road, London SW7 2AZ, United Kingdom.

[2]Institut des Sciences Chimiques de Rennes, UMR CNRS 6226, Université de Rennes 1, 263 Avenue du Général Leclerc, 35042 Rennes, France.

[3] Univ. Grenoble Alpes, CNRS, G-INP, LEPMI, F-38000, Grenoble, France.

[4]The ISIS Facility, STFC Rutherford Appleton Laboratory, Harwell Campus, Didcot, OX11 0QX, UK.

ABSTRACT

The *A*-site cation disordered perovskite oxide, $Nd_{0.5}Ba_{0.5}MnO_3$, a precursor of promising electrode materials for Solid Oxide Fuel Cells (SOFCs), has been prepared by heating the *A*-site-ordered and vacancy ordered layered perovskite, $NdBaMn_2O_5$, in air at 1300 °C for 5 h. Both neutron powder diffraction (NPD) and transmission electron microscopy (TEM) showed that $Nd_{0.5}Ba_{0.5}MnO_3$ has a pseudotetragonal unit cell with orthorhombic symmetry (space group *Imma*, $\sqrt{2}\ a_p \times 2\ a_p \times \sqrt{2}\ a_p$) at 20 °C due to antiphase tilting distortion of the MnO_6 octahedra, with the cell dimensions a = 5.503(1) Å, b = 7.7962(4) Å, c = 5.502(1) Å. *In-situ* NPD showed that the oxygen content of $Nd_{0.5}Ba_{0.5}MnO_3$ decreases on heating under 5 vol. % H_2/He flow to ~ 2.50/f.u. at 600 °C while the symmetry becomes cubic. On further heating, the oxygen stoichiometry remains unchanged up to T ~ 800 °C at which point localisation of the oxygen vacancies in the lanthanide layer as well as ordering of the Nd and Ba cations proceeds converting $Nd_{0.5}Ba_{0.5}MnO_{2.5}$ to a layered $NdBaMn_2O_5$ double perovskite. Impedance spectroscopy measurements for the electrode material, $NdBaMn_2O_6$, screen printed on a $Ce_{0.9}Gd_{0.1}O_{2-\delta}$ (CGO) electrolyte showed promising electrochemical performance with polarization resistance of 1.09 Ω cm^2 at 700 °C in air without any optimization.

Keywords: *In-situ* neutron diffraction**,** *A*-site cation ordering, double perovskite manganites, cation order-disorder phase transition, SOFC electrodes, electrochemical impedance spectroscopy (EIS).

1. Introduction

Owing to their excellent mixed-ionic and electronic conductivity and fast oxygen kinetics, layered double perovskite cobaltites, $LnBaCo_2O_5$ (*Ln* = lanthanide), exhibit excellent properties as air electrodes for solid oxide cells (SOCs)[1-4]. The related layered manganites, such as $PrBaMn_2O_5$ and $NdBaMn_2O_5$ were shown to exhibit high performance as a fuel electrode with good redox stability and tolerance to coking and sulphur contamination from hydrocarbon fuels[5, 6]. A noteworthy feature of these manganites is the flexibility of the manganese environment which can vary from 5- to 6-fold coordination. These layered manganites are stable to redox cycling between air and diluted hydrogen atmosphere up to at least 850°C. In air, the phase is oxidised to *A*-site ordered $NdBaMn_2O_6$ (*P*4/*mmm*) whereas it is reduced back to $NdBaMn_2O_5$ in anode operating conditions within the formation of the intermediate metastable ordered orthorhombic phase, $NdBaMn_2O_{5.5}$[7]. Therefore, the $LnBaMn_2O_{5+\delta}$ materials are suitable as both fuel and oxygen electrodes in symmetrical SOCs[5]. This novel concept has significant advantages compared to traditional configurations, regarding both fabrication and maintenance/operation The reduced phase, $LnBaMn_2O_5$, can be fabricated by annealing the *A*-site cation disordered materials, $Ln_{0.5}Ba_{0.5}MnO_{3-\delta}$ under a hydrogen atmosphere at T ~ 800-900 °C[5]. Cation order plays a critical role in mediating the stability and physical properties of these oxides, such as high electrical conductivity and mechanical compatibility. Indeed, fast anion mobility in $LnBaM_2O_5$ (*M* = Co, Mn) is mediated

by *Ln*/Ba ordering[8, 9]. Considering the use of these materials in electrochemical devices, cell manufacture which involves co-sintering of the electrode and electrolyte in air[6] can alter *A*-site ordering resulting in formation of the disordered phase, $Ln_{0.5}Ba_{0.5}MnO_{3-\delta}$[8, 9]. In order to mimic this thermal treatment, a $NdBaMn_2O_5$ layered perovskite was sintered in air at 1300 °C for 5 hours and the *A*-site cation disordered phase so obtained was subsequently heated under hydrogen flow to monitor by *in-situ* neutron powder diffraction the disorder/order structural transition that proceeds under anode SOFC working conditions. Since the $NdBaMn_2O_6$ electrode material is thermally and mechanically stable with ceria electrolytes[6, 10, 11], impedance spectroscopy measurements for a thin layer screen printed on a $Ce_{0.9}Gd_{0.1}O_{2-\delta}$ (CGO) electrolyte were performed in the temperature range of 500-800 °C to evaluate its electrochemical performance as an oxygen electrode for SOCs.

2. Experimental

A polycrystalline oxygen-deficient perovskite sample (~ 5 g) with layered ordering of Nd and Ba referred to as $NdBaMn_2O_{5+\delta}$ hereafter, was prepared *via* the citrate-nitrate synthesis route as described elsewhere[12]. Part of the $NdBaMn_2O_{5+\delta}$ sample was heated in air at 1300 °C for 5 h to obtain the *A*-site disordered phase, referred to as $Nd_{0.5}Ba_{0.5}MnO_3$ hereafter. Phase purity of both disordered and ordered samples was assessed from powder X-ray diffraction measurements (XRD) at room temperature over the range $10 \leq 2\theta \leq 120°$, $\Delta 2\theta = 0.02°$ using a Bruker AXS D8 Advance diffractometer in Bragg-Brentano geometry equipped with Ge (1 1 1) Johansson-Guinier focusing primary monochromator (Cu-$K\alpha_1$ radiation) and a silicon strip Lynxeye detector. The XRD patterns were analysed using the Rietveld method with the FullProf software[13]. The microstructure of the $Nd_{0.5}Ba_{0.5}MnO_3$ phase was probed by means of transmission electron microscopy (TEM) using a JEOL 2100 LaB_6 instrument operating at 200 kV double tilt (±20°) (point resolution 0.17 nm), fitted with a XEDS microanalysis

system (OXFORD INCA) and ENFINA spectrometer with an energy resolution of 1.3 eV. The sample was crushed in dry ethanol and a few drops of the suspension were deposited on a carbon-coated film (copper grid). Diffraction patterns were collected with a GATAN Orius 200D Charge Coupled Device (CCD) camera. *In-situ* neutron powder diffraction data were collected on the high-flux medium resolution POLARIS diffractometer at ISIS, the UK spallation source at the Rutherford Appleton Laboratory. Approximately 4 g of $Nd_{0.5}Ba_{0.5}MnO_{3-\delta}$ powder was loaded to a depth of 4 cm (corresponding to the height of the incident neutron beam) in a double-walled quartz glass cell built to enable gas to flow through the sample. The cell was mounted in a furnace designed for neutron diffraction measurements and connected to an external gas-handling system to control the oxygen content and flow as the sample was heated to 900 °C in 5% H_2/He gas, allowing the structural stability under anode SOFC operation conditions to be probed directly. The temperature profile used is illustrated schematically in Fig. 1.

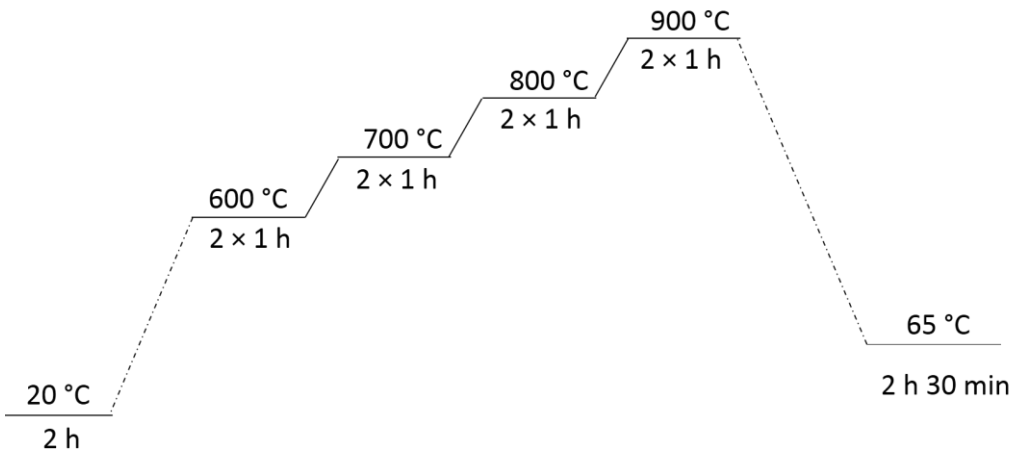

Fig.1. Thermal profile used in the neutron diffraction experiment under 5% H_2/He flow to convert the *A*-site disordered $Nd_{0.5}Ba_{0.5}MnO_{3-\delta}$ phase to A-site ordered $NdBaMn_2O_{5+\delta}$ phase. Heating and cooling rates are 10 °C min^{-1}.

Two thermocouples were attached on opposite sides of the wall of the (inner) quartz tube approx. 5 mm above the sample to control the furnace temperature and monitor the sample temperature. Data normalization and file output was undertaken using the Mantid software

package[14]. The patterns from two banks of detectors; the backscattering bank (average 2θ = 146.7°) which covers a range in 2θ from 135 to 167° with a *d*-spacing range of 0.2-2.65 Å and the 90° bank (average 2θ = 92.6°) which covers a 2θ range of 75 to 113° with a maximum *d*-spacing of 4.1 Å were used together for structure refinement by the Rietveld method, using the FullProf Suite [13]. Peak shapes were modeled by a convolution of two back-to-back exponentials with a pseudo-Voigt function. The background arising from the amorphous quartz glass cell was fitted by the Fourier filtering technique. In addition to the profile parameter (σ_1) describing the Gaussian contribution to the Bragg peak profiles, lattice parameters, fractional occupancy of oxygen sites, atomic positions and isotropic atomic displacement parameters (ADP) were refined. Any additional constraints are noted when describing specific models.

The electrochemical properties of an oxidised $NdBaMn_2O_6$ phase were measured by electrochemical impedance spectroscopy (EIS) in air. The $NdBaMn_2O_6$ phase was obtained by topotactic oxidation of $NdBaMn_2O_5$ in air at T ~ 500 °C for 5 hours, as described previously[12]. This temperature is low enough to avoid any changes in the *A*-site distribution. The ink was prepared by mixing the polycrystalline $NdBaMn_2O_6$ powder with a commercial dispersant (KD2921, Zschimmer and Schwarz). The film was deposited on a $Ce_{0.9}Gd_{0.1}O_{2-\delta}$ (CGO) electrolyte, 19.6 mm in diameter and 1.4 mm thick, by the screen printing technique (SP) then annealed at 700 °C for 3 h in air to increase overall crystallinity and improve interface bonding with the electrolyte. The EIS measurements were carried out using an Autolab potentiostat-galvanostat (PGSTAT 302N) in the temperature range 500 °C - 700 °C at 50 °C intervals and with a frequency range of 0.05 Hz - 100 kHz. The measurements were performed with a signal amplitude of 0.02 V at open circuit potential (OCP), using gold grids (Heraeus, woven gauzes, 1024 meshes per cm^2 and a wire diameter of 0.06 mm) as the current collectors. The EIS data were normalized to the electrode surface area (A = 1.54 cm^2) and

fitted using equivalent circuits with the ZView® software (Scribner Associates). The polarization resistance, R_{pol}, values were calculated by subtracting the high frequency (HF) intercept from the low frequency (LF) intercept on the real axis of the electrode impedance on the Nyquist plane. Since the measurements were performed on symmetrical cells, the obtained R_{pol} values were calculated as follows; $(R_1+R_2) \times A / 2$, where R_1 and R_2 are the HF and LF contributions, respectively.

3. Results and discussion

The initial characterisation of the $NdBaMn_2O_{5+\delta}$ sample heated in air at $T \sim 1300$ °C was carried out by X-ray diffraction recorded at 20 °C. The diffraction pattern shows the presence of the main *A*-site disordered manganite phase, $Nd_{0.5}Ba_{0.5}MnO_3$, and a minor hexagonal perovskite impurity, $BaMnO_{3-\delta}$[2, 15] (Fig. 2). Although the pattern of $Nd_{0.5}Ba_{0.5}MnO_3$ can be indexed using a cubic unit cell, as reported previously[2], lower symmetry was suggested from transmission electron microscopy (TEM) and neutron powder diffraction (NPD). Therefore, indexing was performed in the orthorhombic *Imma* space group on the basis of NPD analysis and in agreement with the symmetry of the related compounds, $Ln_{0.7}Ba_{0.3}MnO_3$ (*Ln* = Pr, Nd)[16], giving the cell parameters, a = 5.503 (1) Å, b = 7.7962 (4) Å, c = 5.502 (1) Å and V = 236.1 (3) Å^3.

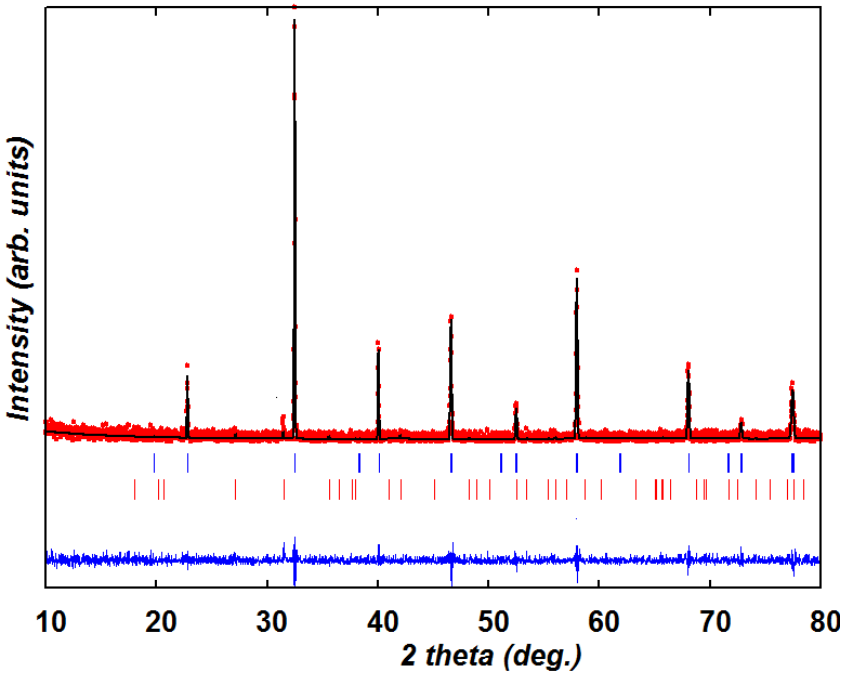

Fig. 2. Fitted room temperature X-ray diffraction pattern of $Nd_{0.5}Ba_{0.5}MnO_{3-\delta}$ phase indexed in *Imma* (upper markers); lower markers correspond to $BaMnO_3$ secondary phase (~ 8 wt %) indexed in $P6_3/mmc$.

3.1 Electron diffraction at room temperature

Fig. 3 shows selected area electron diffraction (SAED) pattern of the $NdBaMn_2O_{5+\delta}$ sample treated in air at 1300 °C. The strong reflections can be indexed on the single perovskite cubic phase and no extra reflections related to the cation ordering along the *c*-lattice parameter were observed.

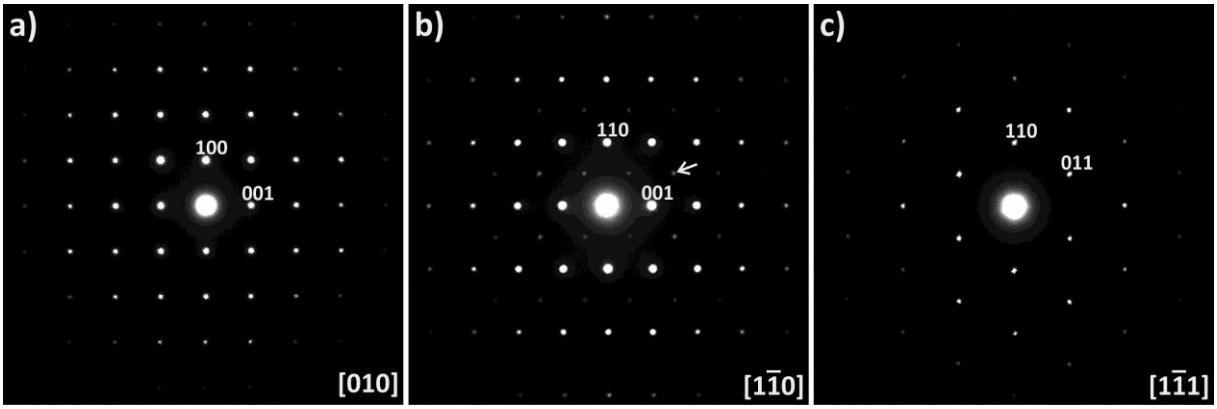

Fig. 3 SAED patterns of $Nd_{0.5}Ba_{0.5}MnO_{3-\delta}$ along the zone axis a) $[010]_p$, b) $[1\bar{1}0]_p$ highlighting by an arrow a superlattice reflection due to tilting of the MnO_6 octahedra network and c) $[1\bar{1}1]_p$. Indexes are in the primitive cubic perovskite structure.

However, ½(*ooo*)$_p$ superlattice reflections (*o* refers to odd Miller indices of the cubic cell), as indicated by an arrow in Fig. 3b, are observed and result from anti-phase tilting of the MnO_6 octahedra network according Glazer[17] and Woodward [18]. Moreover, no ½(*ooe*)$_p$ superlattice reflections (*e* refers to even Miller indexes) are observed in Fig. 3a and 3b suggesting no evidence of in-phase tilting. As a result, the ½(*ooo*)$_p$ reflections can be described in six space groups (S.G.) [17, 19]: *I4/mcm* ($a^0a^0c^-$), *Imma* ($a^0b^-b^-$), *R*$\bar{3}$*c* ($a^-a^-a^-$), *C2/m* ($a^0b^-c^-$), *C2/c* ($a^-b^-b^-$) *and P*-1 ($a^-b^-c^-$)[18]. Since barium perovskite manganites usually crystallise in *I4/mcm* or *Imma*[16], both groups have been evaluated on the basis of NPD patterns collected in this study.

3.2 Neutron diffraction on heating/cooling under dry 5% H_2 /He

The neutron diffraction patterns collected at 20 °C from the sample treated in air at 1300 °C reveal the presence of a main perovskite phase, $Nd_{0.5}Ba_{0.5}MnO_{3-\delta}$ whose pattern could be indexed either in a tetragonal *I4/mcm* ($\sqrt{2}\ a_p \times \sqrt{2}\ a_p \times 2\ a_p$) or orthorhombic *Imma* ($\sqrt{2}\ a_p \times 2\ a_p \times \sqrt{2}a_p$) cell where a_p refers to the lattice parameter of the primitive cubic perovskite structure. Both space groups (S.G.) comprise two oxygen sites; O1 within the Nd/Ba layer and O2 within the Mn layer. Quite similar fits to the NPD data were obtained in both *I4/mcm* ($\chi^2 \sim 1.56$) and *Imma* ($\chi^2 \sim 1.50$) space groups but the latter reproduced the patterns better (Fig. 4) and was consistent with that reported for the $Ln_{0.7}Ba_{0.3}MnO_3$ and $Ln_{0.9}Ba_{0.1}MnO_3$ (*Ln* = Pr, Nd) manganites[16]. However, we stress that unambiguous determination of the S.G. of $Nd_{0.5}Ba_{0.5}MnO_3$ is complicated since the detection of superlattice peaks or resolution of the splitting of the fundamental reflections is impossible due to the resolution limits of Polaris ($\Delta d/d = 10^{-3}$) combined with poor statistics and the background originating from the quartz cell.

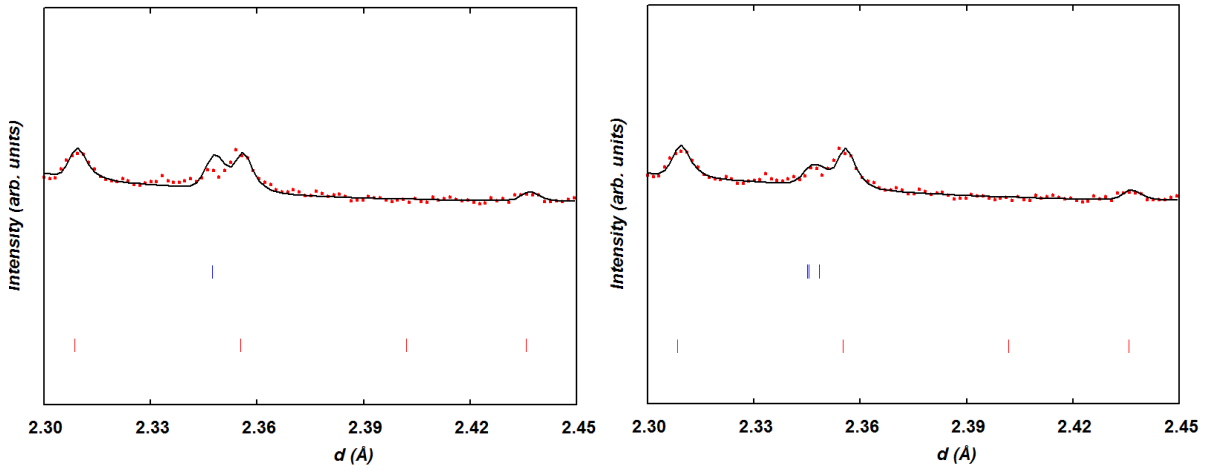

Fig. 4 Part of the NPD data collected at 20 °C for $Nd_{0.5}Ba_{0.5}MnO_{3-\delta}$ comparing the fits at d ~ 2.35 Å (left) S.G. *I*4/*mcm* and (right) S.G. *Imma* ; lower markers relate to the hexagonal $BaMnO_3$ phase (S.G. $P6_3/mmc$).

The site occupation factor at the O1 and O2 sites in $Nd_{0.5}Ba_{0.5}MnO_{3-\delta}$ refined to ~ 1.00 and ~ 0.97(1), respectively, resulting in an overall calculated oxygen content of ~ 2.94(2). Bond angle and distance calculations show octahedral tilting angles Mn-O1-Mn = 170.2(5) °, Mn-O2-M =175.3(5) ° and similar Mn-O bond lengths; Mn-O1 = 1.9562 (9) Å, Mn-O2 = 1.9477 (5) Å. The crystal structure of $Nd_{0.5}Ba_{0.5}MnO_{3-\delta}$ and the full Rietveld fit are displayed in Fig. 5 while the structural parameters and agreement factors are listed in Table 1.

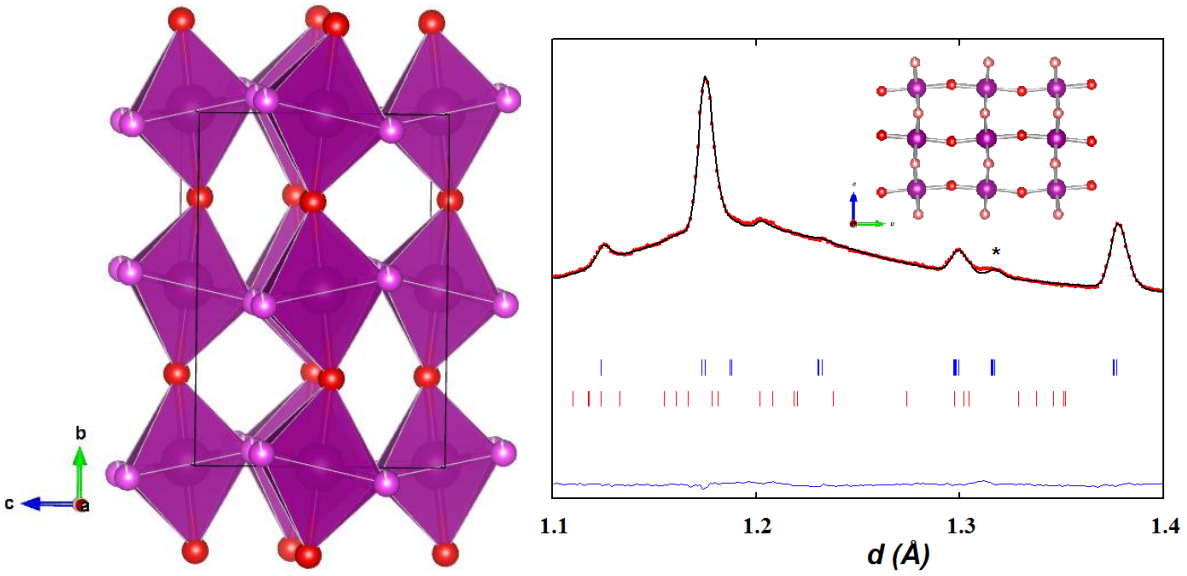

Fig. 5 (left) orthorhombic *Imma* $Nd_{0.5}Ba_{0.5}MnO_{3-\delta}$ structure with two independent oxygen sites with (red) O1 (0, 0.25, *z*) and (pink) O2 (0.25, *y*, 0.25); (right) NPD patterns recorded at 20 °C from the 90° bank for the air treated sample; $Nd_{0.5}Ba_{0.5}MnO_{3-\delta}$ ~ 92 wt % (upper markers) and $BaMnO_3$ ~ 8 wt % (lower markers). The peak labelled (*) is a superlattice reflection not indexed in cubic $Pm\bar{3}m$.

Table 1. Refined lattice parameters and isotropic atomic displacement parameter (B_{iso}) for $Nd_{0.5}Ba_{0.5}MnO_{3.00}$ (S.G. *Imma*) at 20 °C with atoms in the following positions: (Nd,Ba), 4*e* (0, 1/4, *z*); Mn, 4*b*(0, 0, 1/2); O1, 4*e*(0, 1/4, *z*); O2, 8*g* (1/4, *y*, 01/4), *a* = 5.503(1) Å, *b* = 7.7962(4) Å, *c* = 5.502(1) Å, V_p = 59.01(2) Å^3, χ^2 ~ 1.92, R_B ~ 1.98 %, R_f ~ 4.45%.

Atom	***z* or *y***	$\boldsymbol{B_{iso}}$ **(Å^2)**
Nd, Ba	0.0	0.56(2)
Mn		0.62(3)
O1	0.470(2)	2.1(2)
O2	0.512(1)	2.5(1)

Besides $Nd_{0.5}Ba_{0.5}MnO_{3-\delta}$ (~ 92 wt %), the sample contains a minor $P6_3/mmc$ hexagonal $BaMnO_3$ phase (~ 8 wt. %) with lattice parameters, *a* = 5.6268 (7) Å and *c* = 9.241(2) Å. This phase commonly forms readily in air during the synthesis of barium manganite perovskites. Fig. 6 shows representative NPD patterns collected isothermally for 1 hour throughout the heating cycle under a 5% H_2/He gas flow and reveal clearly two successive phase changes; from pseudotetragonal $Nd_{0.5}Ba_{0.5}MnO_3$, to cubic $Nd_{0.5}Ba_{0.5}MnO_{2.5}$ and tetragonal $NdBaMn_2O_5$. At *T* ~ 600°C, the structure of the majority phase has clearly transformed to cubic $Pm\bar{3}m$ and the oxygen content refined to ~ 2.54(4)/f.u. The ratio of the hexagonal phase remained unchanged (~ 6 wt %) while a MnO impurity (< 1 wt %) is also included in the refinement.

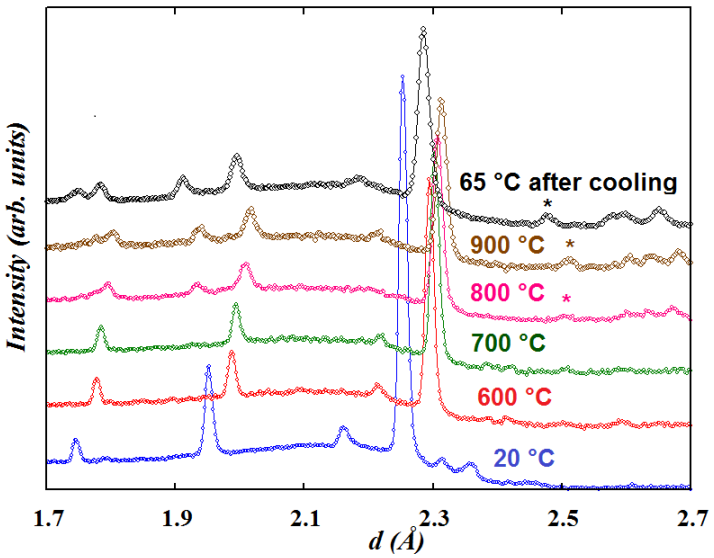

Fig. 6 A section of the observed neutron diffraction patterns of $Nd_{0.5}Ba_{0.5}MnO_{3-\delta}$ recorded in the 90° detector bank at selected temperatures throughout the heating and cooling cycle under 5% H_2/He flow. The disorder-order phase transition proceeds at T ~ 800 °C. The peak labelled (*) arises from SiO_2 of the quartz tube.

Additional data were recorded at T ~ 700 ºC with no changes occurring at this temperature, as revealed by the Rietveld plots displayed in Fig. 7 and structural parameters listed in Table 2.

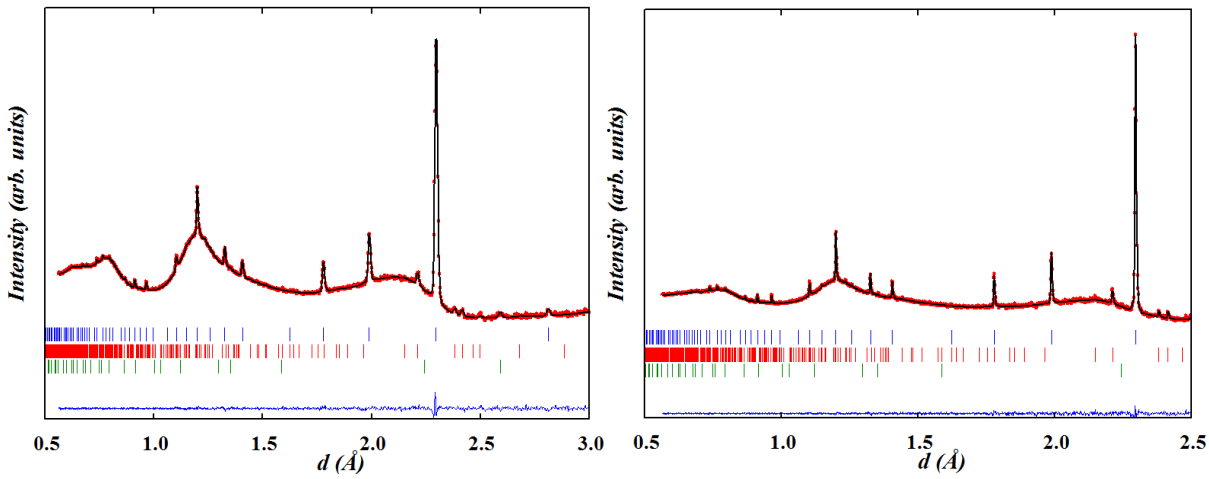

Fig. 7. Rietveld fits to the data collected at T ~ 700 °C for 2 h from (left) 90 ° bank and (right) backscattering-bank. Bragg peaks correspond to $Nd_{0.5}Ba_{0.5}MnO_{2.50}$, S.G. $Pm\bar{3}m$ (upper markers), $BaMnO_{3-\delta}$, S.G. $P6_3/mmc$ (middle markers) and MnO, S.G. $Fd\bar{3}m$ (lower markers).

Table 2. Refined structural parameters and anisotropic thermal vibration parameters B_{ii} for $Nd_{0.5}Ba_{0.5}MnO_{2.5}$ (S.G. $Pm\bar{3}m$) at T ~ 700 °C 700 °C with atoms in the following positions: Nd,Ba 1*a* (0, 0, 0); Mn, 1*b* (1/2, 1/2, 1/2); O, 3*c* (0, 1/2, 1/2).

Atom	B_{11}, B_{22}, B_{33} ($\times 10^3$)
Nd, Ba	44(1), 44(1) 44(1)
Mn	29(1), 29(1), 29(1)
O	39(2), 154(2), 154(2)

The large anisotropy of thermal vibrations for the oxygen atoms originates principally from the dynamic disorder suggesting large mobility and lability. The cubic structure of $Nd_{0.5}Ba_{0.5}MnO_{2.5}$ is unstable as oxygen-vacancy ordering proceeds at ~ 800 °C causing a phase transformation to tetragonal $NdBaMn_2O_5$ (Fig. 8) while the hexagonal $BaMnO_3$ phase has completely disappeared. Ordering of anion vacancies reduces the coordination of the *A* sites producing two different *A*-site coordination geometries; 12 and 8 occupied by the Ba and Nd ions respectively. The first dataset recorded for 1 hour at 800 °C can be modelled assuming the coexistence of three phases $NdBaMn_2O_5$, *P*4/*mmm* (~ 68 wt %), $Nd_{0.5}Ba_{0.5}MnO_{2.5}$, $Pm\bar{3}m$ (~ 30 wt %) and MnO (~ 2 wt %) whose ratios are difficult to estimate accurately because of peak overlay and background approximations. An extra peak labelled (*) emerges at d ~ 2.50 Å (Fig. 9) whose intensity increases on further heating and likely arises from crystallization of SiO_2 from the quartz tube. The conversion of $Nd_{0.5}Ba_{0.5}MnO_{2.5} \rightarrow NdBaMn_2O_5$ is slow because it involves phase separation into two distinct forms and requires nucleation and growth of a different crystal structure. The effect is illustrated by the presence of a significant amount of cubic perovskite (~ 20 wt %) in the second dataset collected at 800 °C. The unit cell volume of the *A*-site ordered phase normalized to the primitive perovskite, V ~ 63.0 Å^3, is similar to that of the oxygen deficient disordered phase, V ~ 63.5 Å^3. The structural parameters of $NdBaMn_2O_5$ at 800 °C are displayed in Table 3 and are consistent with those reported previously[12].

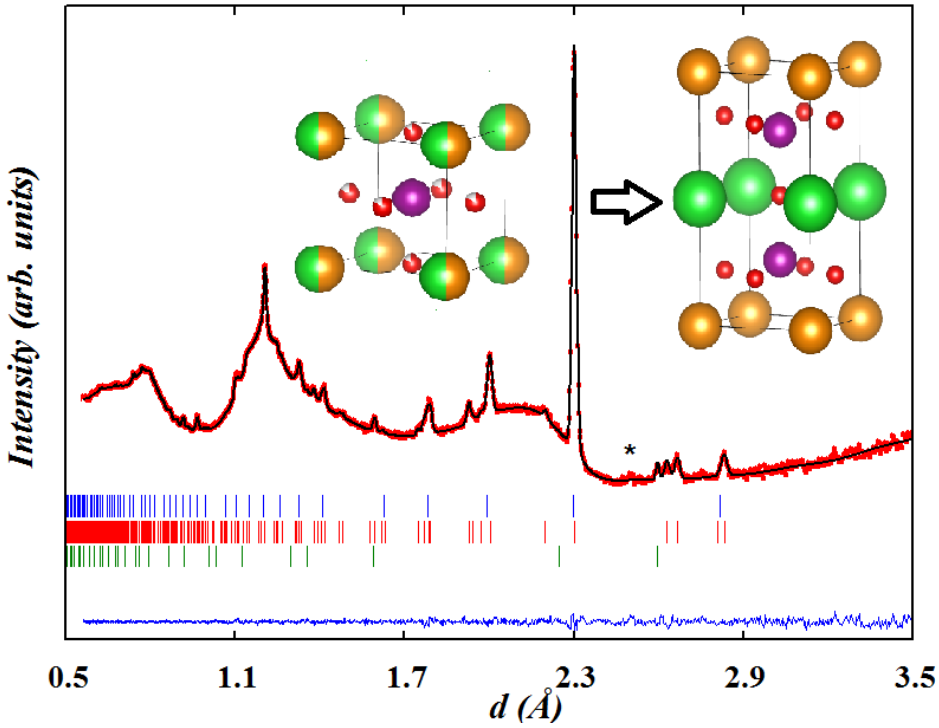

Fig. 8. Rietveld fits to the dataset collected at 800 °C in the 90 °detector bank. Bragg peaks correspond to $NdBaMn_2O_5$, *P*4/*mmm* (upper markers), $Nd_{0.5}Ba_{0.5}MnO_{2.50}$, S.G. $Pm\bar{3}m$ (middle markers) and MnO, S.G. $Fd\bar{3}m$ (lower markers). The extra peak at *d* ~ 2.5 Å labeled (*) likely arises from crystallised SiO_2 of the quartz tube.

Table 3. Refined structural parameters and anisotropic thermal vibration parameters B_{ii} at 800 °C for $NdBaMn_2O_5$ in space group *P*4/*mmm* with atoms in the following positions: Nd, 1*a* (0, 0, 0); Ba, 1*b* (0, 0, 1/2); Mn, 2*h* (1/2, 1/2, z); O1, 1*d* (1/2, 1/2, 1/2); O2, 4*i* (1/2, 0, *z*); *a* ~ 4.0066(5) Å, *c* ~ 7.889(1) Å, χ^2 ~ 1.0, R_B ~ 4 %, R_F ~ 8 %.

Atom	B_{11}, B_{22}, B_{33} ($\times 10^3$)
Nd	22(2), 22(2) 5(1)
Ba	27(3), 27(2), 4(1)
Mn	25(2), 25(2), 8(1)
O1	106(6), 106(6), 4(1)
O2	41(3), 31(2), 27(1)

At T ~ 900 °C, the kinetics increase and the cubic phase has completely transformed into the *A*-site ordered phase (Fig. 9) while the MnO content remains constant at ~ 2 wt %. The phase transformation may proceed with nucleation and subsequent growth of the generated phase rather than by a diffusion-controlled process.

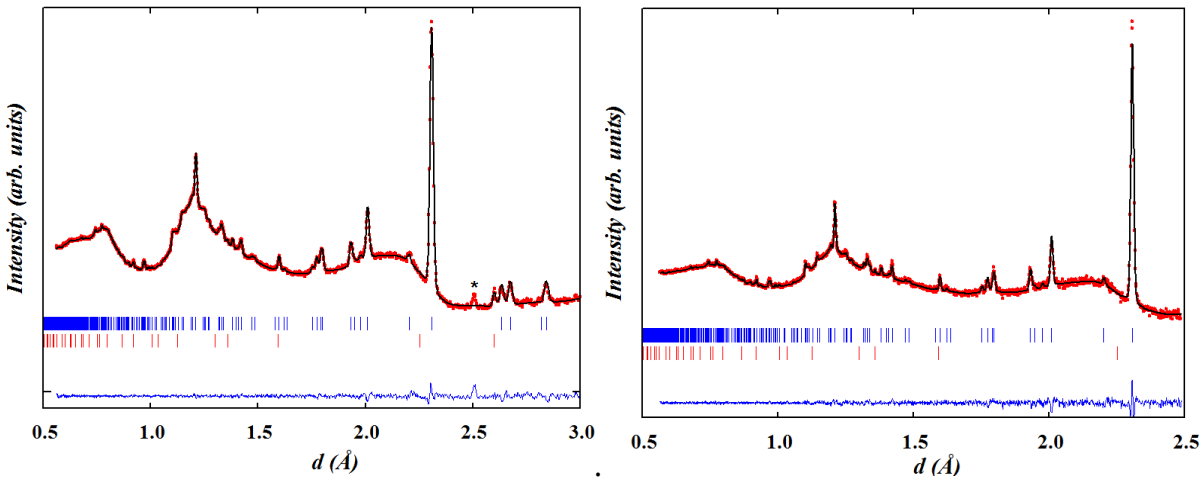

Fig. 9. Rietveld fits to data collected at 900 °C for 2 hours from the (left) 90 ° detector bank and (right) backscattering-bank. Bragg peaks correspond to $NdBaMn_2O_5$ *P*4/*mmm* (upper markers) and MnO $Fd\bar{3}m$ (lower markers). The unindexed peak at d ~ 2.5 Å is labelled (*).

Although the *P*4/*mmm* and *P*4/*nmm* models gave equivalent fits (χ^2 ~ 2.0) to the neutron data collected at 65 °C for 2.5 h after cooling, the charge ordered model was adopted in agreement with our previous study. The large width of the diffraction peaks reflects a substantial decrease in the crystallite size of the polycrystalline ordered compound that is consistent with ordering of the Nd^{3+}/Ba^{2+} cations and oxygen vacancies. The normalized unit cell volume of $NdBaMn_2O_5$, V ~ 61.5 $Å^3$, is larger than that of $Nd_{0.5}Ba_{0.5}MnO_{3.0}$, V ~ 59.0 $Å^3$ as expected when oxygen is removed from the structure. The Rietveld fit to the data collected after cooing to 65°C using space group *P4/nmm* is displayed in Fig. 10 and the structural parameters and agreement factors are listed in Table 4. The oxygen content was fixed at the value refined from the 900 °C data set. The additional peak that originates from SiO_2 is still present and was not observed in our previous experiment[12] in which heating was limited to a temperature of 800 °C.

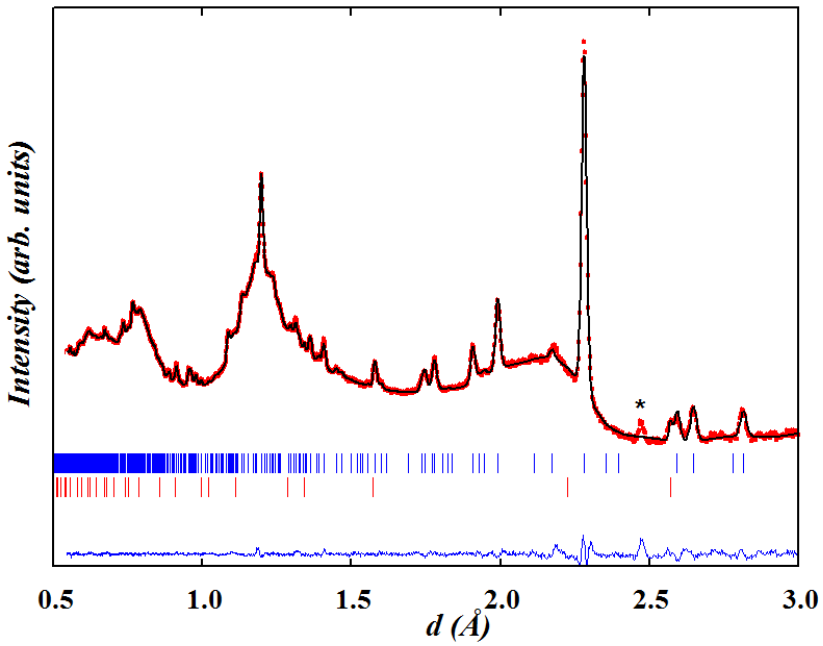

Fig. **10**. Rietveld fit to the data collected for 2 h in the 90° detectors after cooling to 65 °C. Bragg peaks correspond to $NdBaMn_2O_5$, S.G. *P*4/*nmm* (upper markers) and MnO, S.G. $Fd\bar{3}m$ (lower markers). The additional peak likely to arise from crystallization of SiO_2 from the quartz tube is labelled (*).

Table 4. Refined structural parameters and isotropic thermal vibration parameters B_{iso} at 65 °C for $NdBaMn_2O_5$ in space group *P*4/*nmm* with atoms in the following positions: Nd, 2b (3/4, 1/4, 1/2); Ba, 2a (3/4, 1/4, 0); Mn1(Mn^{2+}), 2*c* (1/4, 1/4, *z*); Mn2(Mn^{3+}), 2*c* (1/4, 1/4, *z*); O1, 2c (1/4, 1/4, *z*); O3, 8*j* (*x*, *x*, *z*); O3, 2*c* (1/4, 1/4, 1/2). B_{iso} for Mn1 and Mn2 were constrained to be equal.

Atom	*a* (Å)	5.6251(4)
	c (Å)	7.7717(7)
Nd	B_{iso} (Å^2)	0.47(4)
Ba	B_{iso} (Å^2)	0.56(7)
Mn1	*z*	0.258(2)
	B_{iso} (Å^2)	0.31(6)
Mn2	*z*	0.756(1)
O1	*z*	0.002(3)
O2	*x*	0.500(2)
	z	0.3077(2)
	B_{iso} (Å^2)	1.38(4)
	χ^2	2.11
	R_B %	5.42

3.3 Electrochemical properties

In this section, the electrochemical properties of screen-printed $NdBaMn_2O_6$ electrodes studied by EIS are presented. The impedance diagrams were analyzed using the ZView® software with an equivalent circuit, consisting of a combination of two resistance (R)-constant phase element (CPE) parallel circuits, connected in series with an inductance (L1) and a series resistance including the ohmic losses originating from electrolyte (Rs), as shown in Fig. 11. This electrical element (L1), appearing as a high frequency tail below the real axis, represents the contribution of the connecting leads, measuring device and connecting wires to the measured total impedance[20]. CGO conductivity of 0.018 S cm^{-1} has been calculated from the data obtained at 600 °C from the R_S value and was found to be in good agreement with the literature[21].

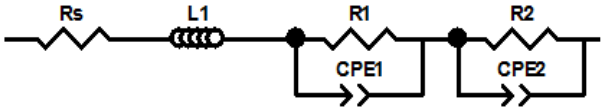

Fig. 11. Equivalent circuit used for the fitting of the electrochemical impedance diagrams.

According to the selected analysis, the electrode response is composed of two main elementary contributions located at high frequency (HF) and low frequency (LF), as shown in Fig. 12a for data recorded at 600 °C. The high frequency contribution (HF) is attributed to charge transfer at the electrode/electrolyte interface whereas the low frequency contribution (LF) can be associated with various electrode processes such as adsorption of gaseous oxygen

O_2, dissociation of O_2 and charge transfer-diffusion (O^{2-}) in the electrode[20-23.]

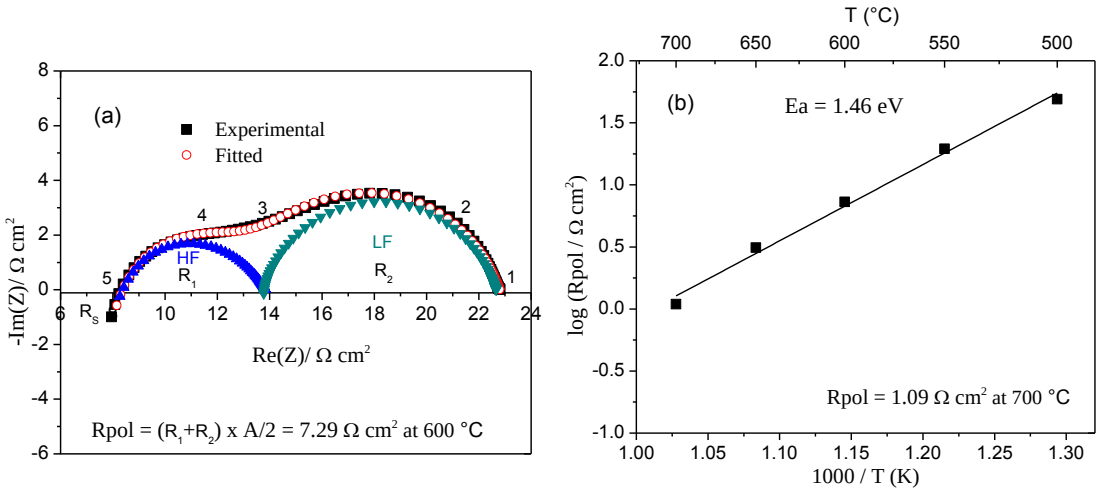

Fig. 12. Electrochemical performance of $NdBaMn_2O_6$ symmetrical cell on CGO electrolyte: Nyquist impedance diagrams at 600 °C in air at OCV (numbers indicate the logarithm of the measuring frequency), (b) Arrhenius plot.

The thermal variations of Polarization resistance, R_{pol}, values are shown in Fig. 12b. R_{pol} decreases with increasing temperature, as expected. The R_{pol} value was found to be 7.29 Ω cm² at 600 °C (1.09 Ω cm² at 700 °C). Activation energy has been found to be 1.46 eV. The R_2 values are always larger than the R_1 ones (as shown in Fig. 12a at 600 °C), suggesting that the oxygen desorption or adsorption process is the rate-limiting step for the oxygen reduction reaction (ORR)[24, 25, 26]. Indeed, $NdBaMn_2O_6$ oxygen electrodes shows similar performance as $La_3Ni_2O_{7+\delta}$ and $La_4Ni_3O_{10-\delta}$ electrodes[27]. However, cathode composition, microstructure and architecture for a given composition plays a very important role in improving the cathode performance[27-34,] For example R. Sayers *et al.* reported R_{pol} values of 1.0 Ω cm² at 700 °C, screen printed (SP) after the addition of a thin and dense $La_2NiO_{4+\delta}$ layer in between SP $La_2NiO_{4+\delta}$ and CGO electrolyte[30]. Sharma *et al.* have recently reported a R_{pol} value of 0.08 Ω cm² at 700 °C for a double layer $La_2NiO_{4+\delta}$ electrode prepared by electrostatic spray deposition technique followed by screen-printing a layer of $La_2NiO_{4+\delta}$ on a CGO electrolyte, which is the reference in the literature at the moment for the pure $La_2NiO_{4+\delta}$[28]. Further

improvement in the cathode performance has been recently reported (R_{pol} value equal to 0.04 Ω cm² was found at 700 °C) by Sharma *et al.* when a $La_2NiO_{4+\delta}$/CGO composite layer was inserted in between a CGO electrolyte and $La_2NiO_{4+\delta}$ cathode[33]. Nicollet *et al.* have also reported similar performance (R_{pol} value equal to 0.05 Ω cm² was found at 700 °C) when $La_2NiO_{4+\delta}$ was infiltrated inside a CGO backbone[34]. Therefore, our future goal is to improve the cathode performance by improving the cathode microstructure, architecture and composition as well as to study the effect of sintering temperature on its performance.

Conclusions

Crystal evolution of the *A*-site disordered manganite, $Nd_{0.5}Ba_{0.5}MnO_3$, has been studied under hydrogen flow as a function of temperature up to 900 °C. $Nd_{0.5}Ba_{0.5}MnO_3$ crystallises in a pseudo-tetragonal orthorhombic cell at room temperature due to tilting of the MnO_6 octahedra. Heating in a dilute hydrogen atmosphere induces oxygen loss leading to the oxygen vacant cubic phase, $Nd_{0.5}Ba_{0.5}MnO_{2.50}$, which retains *A*-site cation disorder up to T ~ 700 °C. On further heating, a structural rearrangement consisting of oxygen vacancy ordering proceeds at T ~ 800 °C along with *A*-site cation ordering resulting in the $NdBaMn_2O_5$ layered perovskite. $NdBaMn_2O_6$ screen printed onto a $Ce_{0.9}Gd_{0.1}O_{2-\delta}$ (CGO) substrate shows promising performance as an oxygen electrode in a solid oxide fuel cell, with polarisation resistance down of 1.09 Ω cm^2 at 700 °C in air.

Acknowledgements

The authors thank Chris Goodway, Paul McIntyre and Adam Sears of the ISIS User Support Group for technical assistance with the furnace and gas handling equipment during the neutron diffraction experiment and STFC for provision of neutron beam time (RB 1510473). We would like to thank Dr Marek Jura for help on the Rigaku Miniflex 600 X-ray powder

diffractometer in the Materials Characterisation Laboratory at the ISIS Neutron and Muon Source, and Dr Craig Bull at ISIS for giving us access to pellet-making facilities and a high temperature furnace for on-site sample preparation. MB acknowledges T. Roisnel (UR1) for fruitful advice for the analysis of TOF data. FT thanks the KAUST Academic Excellence Alliance for funding.

References

1. M. Burriel, J. Peña-Martínez, R. J. Chater, S. Fearn, A. V. Berenov, S. J. Skinner and J. A. Kilner, *Chemistry of Materials*, 2012, **24**, 613-621.
2. T. Broux, M. Bahout, J. M. Hanlon, O. Hernandez, S. Paofai, A. Berenov and S. J. Skinner, *Journal of Materials Chemistry A*, 2014, **2**, 17015-17023.
3. Y. Hu, O. Hernandez, T. Broux, M. Bahout, J. Hermet, A. Ottochian, C. Ritter, G. Geneste and G. Dezanneau, *Journal of Materials Chemistry*, 2012, **22**, 18744-18747.
4. M. Bahout, S. S. Pramana, J. M. Hanlon, V. Dorcet, R. I. Smith, S. Paofai and S. J. Skinner, *Journal of Materials Chemistry A*, 2015, **3**, 15420-15431.
5. S. Sengodan, S. Choi, A. Jun, T. H. Shin, Y.-W. Ju, H. Y. Jeong, J. Shin, J. T. S. Irvine and G. Kim, *Nat Mater*, 2015, **14**, 205-209.
6. O. L. Pineda, Z. L. Moreno, P. Roussel, K. Świerczek and G. H. Gauthier, *Solid State Ionics*, 2016, **288**, 61-67.
7. F. Tonus, M. Bahout, V. Dorcet, G. H. Gauthier, S. Paofai, R. I. Smith and S. J. Skinner, *Journal of Materials Chemistry A*, 2016, **4**, 11635-11647.
8. A. A. Taskin, A. N. Lavrov and Y. Ando, *Progress in Solid State Chemistry*, 2007, **35**, 481-490.
9. A. A. Taskin, A. N. Lavrov and Y. Ando, *Applied Physics Letters*, 2005, **86**, 091910-091913.
10. H. Hayashi, M. Kanoh, C. J. Quan, H. Inaba, S. Wang, M. Dokiya and H. Tagawa, *Solid State Ionics*, 2000, **132**, 227-233.
11. M. S. Kaluzhskikh, S. M. Kazakov, G. N. Mazo, S. Y. Istomin, E. V. Antipov, A. A. Gippius, Y. Fedotov, S. I. Bredikhin, Y. Liu, G. Svensson and Z. Shen, *Journal of Solid State Chemistry*, 2011, **184**, 698-704.
12. F. Tonus, M. Bahout, V. Dorcet, G. H. Gauthier, S. Paofai, R. I. Smith and S. J. Skinner, *Journal of Materials Chemistry A*, 2016, DOI: 10.1039/C6TA03224A.
13. J. Rodríguez-Carvajal, *Physica B: Condensed Matter*, 1993, **192**, 55-69.
14. Mantid, *Manipulation and Analysis Toolkit for Instrument Data. Mantid Project*, 2013.
15. T. Nakajima, H. Kageyama and Y. Ueda, *Journal of Physics and Chemistry of Solids*, 2002, **63**, 913-916.
16. S. Trukhanov, V. Khomchenko, L. Lobanovski, M. Bushinsky, D. Karpinsky, V. Fedotova, I. Troyanchuk, A. Trukhanov, S. Stepin, R. Szymczak, C. Botez and A. Adair, *Journal of Experimental and Theoretical Physics*, 2006, **103**, 398-410.
17. A. M. Glazer, *Acta Crystallographica B* 1972, **28**, 3384-3392.
18. I. M. Reaney and D. I. Woodward, *Acta Crystallographica Section B*, 2005, **61**, 387-399.
19. A. M. Glazer, *Acta Crystallographica Section A*, 1975, **31**, 756-762.
20. C. Fu, K. Sun, N. Zhang, X. Chen and D. Zhou, *Electrochimica Acta*, 2007, **52**, 4589-4594.

21. B. C. H. Steele, *Solid State Ionics*, 2000, **129**, 95-110.
22. S. B. Adler, *Solid State Ionics*, 2000, **135**, 603-612.
23. M. J. Escudero, A. Aguadero, J. A. Alonso and L. Daza, *Journal of Electroanalytical Chemistry*, 2007, **611**, 107-116.
24. Z. Lou, J. Qiao, Y. Yan, J. Peng, Z. Wang, T. Jiang and K. Sun, *International Journal of Hydrogen Energy*, 2012, **37**, 11345-11350.
25. S. Huang, Q. Lu, S. Feng, G. Li and C. Wang, *Advanced Energy Materials*, 2011, **1**, 1094-1096.
26. H. Gu, H. Chen, L. Gao, Y. Zheng, X. Zhu and L. Guo, *International Journal of Hydrogen Energy*, 2009, **34**, 2416-2420.
27. R. K. Sharma, M. Burriel, L. Dessemond, J.-M. Bassat and E. Djurado, *Journal of Power Sources*, 2016, **325**, 337-345.
28. R. K. Sharma, M. Burriel, L. Dessemond, V. Martin, J.-M. Bassat and E. Djurado, *Journal of Power Sources*, 2016, **316**, 17-28.
29. R. K. Sharma, S.-K. Cheah, M. Burriel, L. Dessemond, J.-M. Bassat and E. Djurado, *Journal of Materials Chemistry A*, 2017, DOI: 10.1039/C6TA08011A.
30. R. Sayers, M. Rieu, P. Lenormand, F. Ansart, J. A. Kilner and S. J. Skinner, *Solid State Ionics*, 2011, **192**, 531-534.
31. V. Vibhu, A. Rougier, C. Nicollet, A. Flura, J.-C. Grenier and J.-M. Bassat, *Solid State Ionics*, 2015, **278**, 32-37.
32. R. K. Sharma, M. Burriel and E. Djurado, *Journal of Materials Chemistry A*, 2015, **3**, 23833-23843.
33. R. K. Sharma, M. Burriel, L. Dessemond, J. M. Bassat and E. Djurado, *Journal of Materials Chemistry A*, 2016, **4**, 12451-12462.
34. C. Nicollet, A. Flura, V. Vibhu, A. Rougier, J. M. Bassat and J. C. Grenier, *Journal of Power Sources*, 2015, **294**, 473-482.